Intellectual Journal of Energy Harvesting and Storage
Vol. 4, No. 1, June 2026, pp. 9~20
ISSN: 2963-6272, DOI: 10.11591/ehs.v4i1.pp9-20

Electrical boundary conditions' influence on a parabolically tapered piezoelectric energy harvester

Avipsa Priyadarshini, Pramod Bakhati, Shashank Shekhar Pradhan, Ishan Gupta, Rakesh Ranjan Chand
Department of Mechanical Engineering, C. V. Raman Global University, Bhubaneswar, India

Article Info

Article history:

Received Nov 12, 2025
Revised Jan 13, 2026
Accepted May 12, 2026

Keywords:

Electrical boundary conditions
Electromechanical coupling
Finite element validation
Parabolic tapering
Piezoelectric energy harvester

ABSTRACT

This research work presents the analytical modeling, simulation, and validation of a parabolically tapered piezoelectric energy harvester (PEH) subjected to different electrical boundary conditions. A fully coupled one-dimensional electromechanical model is formulated using Euler–Bernoulli beam theory, incorporating variable bending stiffness, mass distribution, and neutral-axis shift arising from the parabolic geometry. The model predicts frequency, voltage, and power response under base excitation and reveals the explicit influence of electrical loading on effective dynamic stiffness. Frequency-domain solutions are validated with ANSYS mechanical ANSYS parametric design language (APDL) simulations, showing less than 2% deviation. Results reveal that open-circuit conditions yield maximum voltage, while optimal power is obtained at a matched resistive load following the impedance matching principle. The parabolic tapering geometry enhances strain uniformity, lowers the resonant frequency, and improves energy conversion efficiency compared to rectangular designs. Parametric studies further demonstrate the impact of taper ratio, harvester length, and piezoelectric thickness on output characteristics. The proposed analytical framework provides a reliable and computationally efficient design tool for low-frequency vibration energy harvesters used in autonomous sensors and internet of things (IoT) applications.

Corresponding Author:

Rakesh Ranjan Chand
Department of Mechanical Engineering, C. V. Raman Global University
Bidyanagar, Mahura, Bhubaneswar 752054, Odisha, India
Email: rakeshranjan.chand@cgu-odisha.ac.in

1. INTRODUCTION

Piezoelectric energy harvesters (PEHs) are widely used for converting ambient mechanical vibrations into electricity, with their performance highly dependent on both structural geometry and electrical boundary conditions [1]–[3]. The electrical boundary condition, such as the type of load resistance or circuit configuration, significantly influences the frequency response and voltage output of these devices. Recent research demonstrates that optimizing electrical boundary conditions, including impedance matching and the use of nonlinear or hybrid circuits, can significantly broaden operational bandwidth, lower resonant frequencies, and increase voltage and power output [4], [5]. Impedance matching is critical for maximizing power transfer, with optimal load resistance yielding peak voltage and power at resonance. Analytical and experimental results confirm that the voltage output peaks at resonance and is sensitive to changes in load resistance [6]. The majority of the research work focuses on the open circuit boundary condition as it gives the maximum voltage output from the gharvester [7]–[9]. But the power from a piezoelectric vibration energy harvester is maximum when the external resistive load equals the internal impedance of the harvester [10]. This

is a direct application of the impedance matching principle, which ensures effective energy transfer from the piezoelectric element to the load. Morel *et al.* [11] tuned the electrical interface of a highly coupled piezoelectric harvester to efficiently harvest energy from ambient vibrations, achieving a maximum power of 11 μW over a 14 Hz wide frequency band with less than 5% error. A coupled piezoelectric-circuit finite element model is used by Zhu *et al.* [12] to analyze the power generating performance of a PEH, attached to a resistive load. The focus was given to understand the effect of the resistance load on the vibration magnitude of the piezoelectric harvester, and thus on the voltage and power output of the device. They also optimized the resistive load and design parameters for maximum power output. Zhu *et al.* [12] optimized the load resistance in their research work and obtained a maximum normalized power density of 18.717 mW/g^2cm^3. Therefore, in this study, the influence of electrical boundary conditions on the piezoelectric harvester's responses.

One of the primary reasons for the inefficiency of commonly used PEHs is the nonuniform stress distribution aroused due to improper harvester design. To address the issue, various geometries have been tried in the past decade. Non-uniform and tapered piezoelectric beams are widely used to tune resonance frequencies, enhance electromechanical coupling, and improve energy harvesting. Recent work combines analytical, semi-analytical, and finite element formulations to study how loads, tapering, and material grading influence dynamic response and stability [13]–[16]. The research diaspora started with simple rectangular geometry, then linearly tapering, exponentially tapering, as well as quadratically tapering profiles were also tried [17], [18]. The researchers [19], [20] introduced a trapezoidal shape cantilever structure for piezoelectric energy harvesting applications. Numerical simulations revealed that the power output could be significantly improved by fine-tuning the design parameters, enabling the system to achieve resonance at any rotational speed. Experimental results demonstrated an average power output of 107.4 mW over a wheel speed range of 177 to 796 RPM. However, the complexity of their design limits their practicality for real-world applications. Deng *et al.* [21] developed a finite element model of a linearly tapering design using ANSYS software. The proposed harvester generated between 5 and 26 mW of power within an operating frequency range of 10–20 Hz. Nevertheless, they did not provide a clear mathematical framework or experimental methodology to predict the energy harvester's performance. Recently, it has been observed that the quadratic and exponentially tapering harvesters provide higher power density and power amplification factor [22], [23]. The design of piezoelectric vibration energy harvesters plays a critical role in determining their efficiency and reliability. Parabolically tapered beams have emerged as a promising design for enhancing energy harvesting efficiency, particularly at low frequencies [24]–[26]. Therefore, the parabolic tapering profile is considered in this study.

The key contributions of this work are:

- A novel electromechanically coupled analytical model for parabolically tapered PEH that incorporates variable stiffness, variable mass, and neutral-axis shift, which are not featured in prior studies.
- The quantitative demonstration of how electrical boundary conditions (open circuit, short circuit, and resistive load) alter effective dynamic stiffness and shift resonance frequencies.
- A complete frequency-domain solution providing voltage and power response under base excitation and different resistive loads, enabling rapid evaluation of matched-load power.
- Validation against ANSYS mechanical ANSYS parametric design language (APDL) for natural frequency, voltage, and power predictions.
- A broad parametric sensitivity analysis, offering guidelines for geometry-electrical co-optimization.
- Comparison with equivalent rectangular geometries, showing advantages of parabolic tapering in strain distribution, lowered resonance, and enhanced energy conversion.

These contributions collectively establish a unified, computationally efficient framework for designing geometry-tailored PEHs for low-frequency energy harvesting and adaptive power conditioning for autonomous sensors and internet of things (IoT) systems.

2. METHOD

2.1. Electro-mechanical coupled mathematical model development

The parabolic tapering width PEH is shown in Figure 1. Figure 1(a) depicts the harvester tapering from base to the free end. The resistive load is assumed to be across the top and bottom layers of the piezoelectric layer. Figure 1(b) shows the cross-sectional view of the system along with the position of the neutral axis. The width variation equation is derived by considering a parabola with focus $(\alpha, 0)$ and $y^2 = 4\alpha x$ as (1);

$$\begin{aligned} w(x) &= w_0 - 2\sqrt{4ax} = w_0 - 4\sqrt{ax} \\ &= w_0\left[1 - 4\sqrt{\left(\frac{a}{w_0^2}\right)x}\right] \\ &= w_0\left(1 - 4\sqrt{\vartheta x}\right), 0 \le x \le l \end{aligned} \tag{1}$$

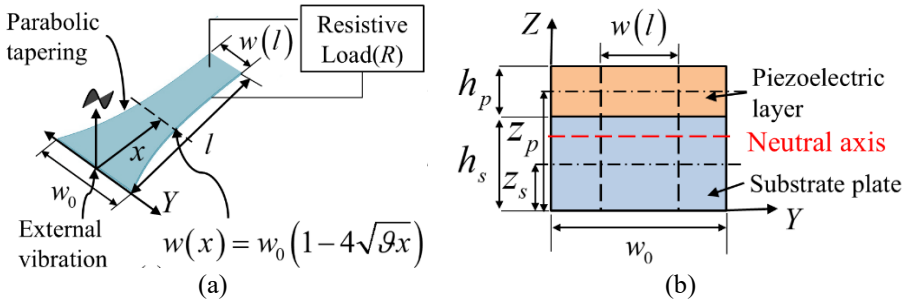

Figure 1. Schematic of the PEH showing; (a) the tapered geometry and (b) the position of neutral axis

where w_0 is the base width of the harvester and $\vartheta = \left(\frac{a}{w_0^2}\right)$ is the taper parameter. The span of the system is l, the thicknesses of the substrate and the piezoelectric layer are h_s and h_p, respectively. Similarly, the $z_s = \frac{h_s}{2}$ is the substrate centroid and $z_p = h_s + \frac{h_p}{2}$ is the piezoelectric layer centroid, gives the exact position of the neutral axis (z_{NA}) of the unimorph system as (2):

$$z_{NA} = \frac{E_s h_s z_s + E_p h_p z_p}{E_s h_s + E_p h_p} \tag{2}$$

where, E_s and E_p are the substrate and piezoelectric layer's modulus of elasticity. In the present study, Euler–Bernoulli beam theory is adopted to model the parabolically tapered PEH. This choice is justified by the slender geometry of the cantilever, for which the length-to-thickness ratio exceeds 20 for all configurations considered. Under such conditions, transverse shear deformation and rotary inertia effects are negligible, and the Euler–Bernoulli assumption of plane sections remaining plane remains valid. The dynamic interaction between the beam's mechanical deformation and the piezoelectric electrical response is represented by the electromechanically coupled Euler–Bernoulli formulation (one-dimensional) as (3):

$$\frac{d^2}{dx^2}\left[EI(x)\frac{d^2\Delta(x,t)}{dx^2}\right] + \rho A(x)\ddot{\Delta}(x,t) - \phi(x)\dot{V}(t) = 0 \tag{3}$$

and the electrical governing as (4);

$$\int_0^l \phi(x)\frac{d^2\Delta(x,t)}{dx^2}dx + C_p\dot{V}(t) + \frac{V(t)}{R} = 0 \tag{4}$$

where $\Delta(x,t)$ is the transverse deflection, $EI(x)$ is the cumulative bending stiffness, $\rho A(x)$ is the mass per unit length, $\phi(x)$ is the electromechanical coupling coefficient (C/m), C_p is the effective capacitance of the piezoelectric layer, and R is the external resistive load for the harvester, which is taken as infinite for the open circuit and zero for the short-circuit condition. Together, (3) and (4) form a fully coupled one-dimensional distributed model that captures both the structural dynamics and the electrical response of the piezoelectric cantilever beam under open-circuit, short-circuit, and resistive loading conditions. The area moment of inertia of the substrate, $I_s(x)$ and piezoelectric layers, $I_p(x)$ are:

$$I_s(x) = \frac{w(x)h_s^3}{12}, I_p(x) = \frac{w(x)h_p^3}{12} \tag{5}$$

and the cumulative bending stiffness is:

$$EI(x) = E_s I_s(x) + E_p I_p^*(x) \tag{6}$$

where $I_p^*(x) = I_p(x) + w(x)h_p z_{pp}^2$. For the unimorph system:

$$z_{pp} = z_p - z_{NA} \tag{7}$$

Finally, the mass per unit length of the system is:

$$\rho A(x) = \rho_s w(x) h_s + \rho_p w(x) h_p \quad (8)$$

where, ρ_s and ρ_p are the substrate and piezoelectric layer's mass density (kg/m^3).
Now considering d_{31} as the piezoelectric strain constant (C/N), the electromechanical coupling distribution is:

$$\phi(x) = d_{31} E_p w(x) h_p z_{pp} \quad (9)$$

and considering ε_T as the permittivity (F/m), the capacitance is:

$$C_p = \int_0^l \frac{\varepsilon_T w(x)}{h_p} dx \quad (10)$$

Assuming the system's transverse deflection is dominated by a single normalized mode shape:

$$\Delta(x,t) = \theta_n(x) q_n(t) \quad (11)$$

where $q_n(t)$ is the modal generalized displacement and $\theta_n(x)$ is an assumed mode shape for the cantilever structure, selected as (12):

$$\theta_1(x) = cosh(\lambda x/l) - cosh(\lambda x/l) - \eta[sinh(\lambda x/l) - sin(\lambda x/l)] \quad (12)$$

With:

$$\eta = \frac{cosh(\lambda l) + cos(\lambda l)}{sinh(\lambda l) + sin(\lambda l)}, \lambda_1 l = 1.875 \quad (13)$$

Substituting this ansatz into the distributed PDEs in (3) and (4), and applying Galerkin projection and integrating over $x\epsilon[0.1]$, an ordinary differential equation system for the modal coordinate and the voltage is obtained. The resulting modal electromechanical are (14) and (15):

$$M_n \ddot{q}_n(t) + K_n q_n(t) - \Theta_n V(t) = 0 \quad (14)$$

$$\Theta_n \dot{q}_n(t) + C_p \dot{V}(t) + \frac{V(t)}{R} = 0 \quad (15)$$

The coefficients of (14) and (15) are:

$$M_n = \int_0^l \rho A(x) \theta_n^2(x) dx \,, K_n = \int_0^l EI(x) \left(\frac{d^2\theta_n(x)}{dx^2}\right)^2 dx \,, \Theta_n = \int_0^l \theta(x) \left(\frac{d^2\theta_n(x)}{dx^2}\right) dx \quad (16)$$

2.2. Frequency-domain reduction and effective mechanical stiffness

After obtaining the normalized system equations, the solutions are obtained by assuming harmonic responses as $q_n(t) = Qe^{j\omega t}$ and $V(t) = Ve^{j\omega t}$. These assumptions result in:

$$[-\omega^2 M_n + K_n]Q - \Theta_n V_0 = 0 \quad (17)$$

$$j\omega\Theta_n Q + \left(j\omega C_p + \frac{1}{R}\right) V_0 = 0 \quad (18)$$

Solving (18) will give:

$$V_0 = \frac{j\omega\Theta_n RQ}{1 + j\omega C_p R} \quad (19)$$

Now, substituting (19) into (17) will give:

$$\left[-\omega^2 M_n + K_n + \frac{(j\omega\Theta_n)^2 R}{1 + j\omega R C_p}\right] Q = 0 \quad (20)$$

The effective dynamic stiffness of the system in (20) is affected by the electrical circuit, which produces a frequency-dependent mechanical term as (21);

$$K_{eff}(\omega) = K_n + K_{ele}(\omega), K_{ele}(\omega) = \frac{(j\omega\Theta_n)^2 R}{1+j\omega R C_p} \quad (21)$$

The complex natural frequency obtained using (21) depends on the resistive load R, and the resonance occurs when $\left[K_{eff}(\omega)\right] = 0$. Now, for the open-circuit case($R \to \infty$), the effective stiffness and natural frequency $(\omega_{n,OC})$ become:

$$K_{eff} = K_n + \frac{\Theta_n^2}{C_p}, \omega_{n,OC} = \sqrt{\frac{K_n \frac{\Theta_n^2}{C_p}}{M_n}} \quad (22)$$

For the short-circuit case $(R \to 0)$, the $K_{eff} = K_n$, therefore (23):

$$\omega_{n,SC} = \sqrt{\frac{K_n}{M_n}} \quad (23)$$

From (22) and (23), it is clear that the shorted electrodes do not add the additional stiffness term as in case of the open-circuit case. Therefore, the open-circuit frequency is likely to be higher than the short-circuit. Then the frequencies (Hz) can be represented as $f_{n,oc} = \frac{\omega noc}{2\pi}$ and $f_{n,SC} = \frac{\omega nsc}{2\pi}$.

2.3. Voltage-frequency response under base acceleration

Since vibration in the system is induced through base acceleration $a_b(t) = \ddot{\omega} e^{j\omega t}$, the coupled becomes (24):

$$\left[-\omega^2 M_n + K_n + \frac{(j\omega\Theta_n)^2 R}{1+j\omega R C_p}\right] X(\omega) = M_n a_b(t) \quad (24)$$

where the mechanical amplitude $X(\omega)$, with damping coefficient ζ, and modal damping $C_n = 2\,\zeta\sqrt{K_n M_n}$, can be written as (25):

$$X(\omega) = \frac{-M_n a_b(t)}{-M_n\omega^2 + j\omega C_n + K_{eff}} \quad (25)$$

Finally, the output voltage $V(\omega)$ and power $P(\omega)$ can be calculated as (26) and (27):

$$V(\omega) = \left[\frac{\omega j \Theta_n R}{1+j\omega R C_p}\right] \quad (26)$$

$$P(\omega) = \frac{|V(\omega)|^2}{2R} \quad (27)$$

The electromechanically coupled modal analysis is done for both open and short-circuit boundary conditions to extract the first three mode shapes and natural frequencies. Then the harmonic analysis is done by applying base accelerations 1 g, 4 g, and 7 g and sweep frequency around each principal resonance. For each electrical boundary condition (open circuit and short-circuit, and sample resistance values), the electrode voltage amplitude and power dissipation for the resistive cases are recorded.

2.4. Model validation in ANSYS mechanical APDL

Figure 2 illustrates the ANSYS mechanical APDL is used to create the parabolic tapering piezoelectric harvester. Using the width variation function in (1), around 200 key points are generated to model the substrate and piezoelectric patch as shown in Figure 2(a). Couple-field piezoelectric tetrahedral SOLID226 elements are used to discretize the system. A fine mesh is generated to ensure simulation accuracy, resulting in a total of over 10,000 elements. The model and the view after implementation of the VOLT and CP commands are shown in Figure 2(b). Table 1 shows the material properties used in the ANSYS simulation and the analytical method. Also, demonstrates the sensitivity of the first natural frequency to the piezoelectric material parameters. The other reasonable dimensions of the system taken in this study are $l = 6\ cm, \vartheta = 0.6, w_0 = 5\ cm$, $h_s = 0.5\ mm, h_p = 0.2\ mm$, and $\zeta = 0.02$. To simulate the open circuit condition, bottom electrode is given zero potential and the top electrode free. The difference between gives the open circuit voltage response.

The short-circuit condition is simulated by tying both top and bottom electrode nodes to same potential (0 V). The resistive load is applied by connecting the electrode pair to an external circuit containing a resistor.

This is done by utilizing the CIRCU94 element, which links electrode node potentials to a circuit branch with resistance R. Modal analysis and harmonic analysis are done across $\pm 20\%$ of the first three natural frequencies. Figure 2(c) represents the stress distribution comparison of the proposed parabolic tapering geometry with a similar rectangular one. The rectangular geometry is obtained by implementing $\vartheta = 0$, which makes $w(x) = w_0$. The length and the base width for both models are kept constant. It can be seen that the parabolic tapering improves the stress distribution over the surface, giving rise to better material utilization and energy harvesting performance compared to conventional designs.

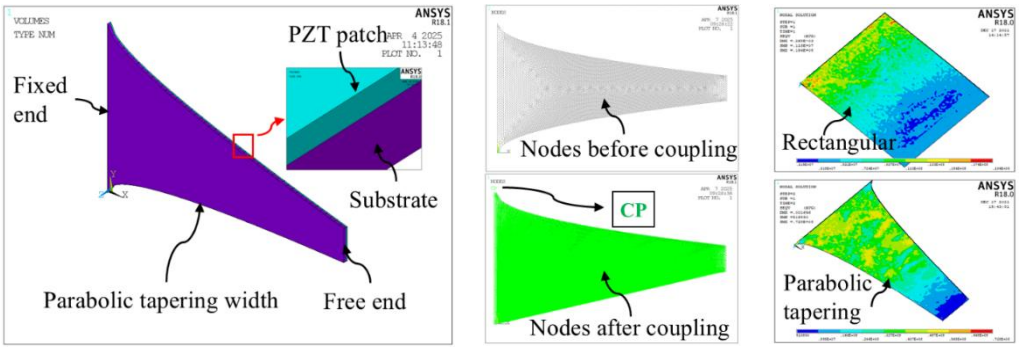

Figure 2. ANSYS model of the system showing; (a) bonded piezoelectric patch and substrate, (b) nodes before and after voltage coupling, and (c) stress distribution comparison of rectangular and parabolic tapering geometry

Table 1. Material properties used in the modelling of the piezoelectric harvester and the sensitivity of the first natural frequency to the piezoelectric material parameters

Properties	PZT-5H patch	Variation (%)	Frequency change (%)	Remarks	Brass substrate
Modulus of elasticity (GPa)	50	±10	5–7	Stiffness dominated change	97
Mass density (kg/m^3)	7960	-	-	-	8490
Poisson's ratio	0.136	-	-	-	0.33
Coupling coefficient (cm^{-2})	-8.939	±10	<1	-	-
Charge constant (C/N)	-320×10^{-12}	±10	<2	Lower influence on stiffness but affects voltage strongly	-
Dielectric constant	3800	±10	<1	-	-
Permittivity (F/m)	-1.306×10^{-10}	±10	<1	Capacitance influence and minimal effect on frequency	-

3. RESULTS AND DISCUSSION

3.1. Model validation

As discussed, a two-way validation process is adopted in this study. First, the results from the analytical model are compared with the ANSYS simulation results. Secondly, the results are compared with the earlier reported results. The ANSYS model presented in subsection 2.4 is simulated under 7 g excitation level, and the results are presented in Table 2. The RMS power is calculated across a resistance of $10^6\ \Omega$ for both cases. The results show close agreement with each other, having relative error percentages of 0.168, 1.363, and 0.190 for the first natural frequency, open circuit voltage, and root mean square (RMS) power, respectively. These minor deviations are considered acceptable, which validates the proposed model. The deviation may have appeared due to the element coupling complexity and material nonlinearities at high excitation levels [26]–[28], which are not considered in the present model.

The results of the present model are compared with some earlier reported rectangular piezoelectric harvester models. The present geometry can be converted into a rectangular shape by implementing the taper parameter as zero, which makes $w(x) = w_0$ for the whole length. The dimensions and material properties of the reported models are utilized in the present model to establish a standard for comparison. The reported and calculated (from the present model) frequencies and RMS powers are compared for validation purposes. Table 3 presents the comparison results along with the used material, excitation level, and piezoelectric patch size. The close agreement (deviation $\leq 3.5\%$) between the reported results further validates the present model.

Table 2. Comparison of analytical and ANSYS simulation results

Method	Output responses		
	Frequency (Hz)	Open circuit voltage (V)	RMS power (μW)
Analytical	130.2184	1.7031	0.5778
ANSYS	130	1.6802	0.5767
% error	0.168	1.363	0.190

Table 3. Comparison of the present analytical model with earlier reported models.

Reference	Material	Excitation (×9.81 m/s^2)	Piezo. size (mm^3)	Frequency (Hz)		RMS power (μW)	
				rep.	cal.	rep.	cal.
Morimoto *et al.* [29]	PZT	0.51	18.5×5×0.28	26.0	128.4	5.30	5.42
Tang *et al.* [30]	PZT	3.0	11×5×0.57	100.8	98.7	3.21	3.10
Song *et al.* [31]	PZT	0.25	11	68.0	70.1	0.023	0.024
Kim *et al.* [32]	PZT-5A	0.255	51×31.7×0.275	109.5	111.6	0.53	0.51
Liang and Liao [33]	PZT-5A	1.44	49×24×0.5	42.0	40.6	0.25	0.26
Xu *et al.* [34]	PMN-PT	3.2	25×5×0.1	102.0	104.8	0.185	0.18
Ma *et al.* [35]	PZT-5H	0.2	30×3×0.3	93.0	95.3	0.318	0.33
Gong *et al.* [36]	PZT	0.7	31×13.6×0.22	120.9	118.2	0.664	0.64

3.2. System response analysis

The mode shapes for natural frequencies and voltage response under open and short-circuit conditions are analyzed in this section to understand the effects of electrical boundary conditions. The RMS power from the piezoelectric harvester against various resistive loads is also studied. To study the effects of base excitation, identical analysis is conducted for 1 g, 4 g, and 7 g excitations.

3.2.1. Frequency response

The first three natural frequencies of the system with open circuit and short-circuit boundary condition is studied to assess the influence of electromechanical coupling. Figure 3 shows the three mode shapes of the harvester with $l = 6$ cm, $\vartheta = 0.6$, $w_0 = 5$ cm, $h_s = 0.5$ mm, $h_p = 0.2$ mm, and $\zeta = 0.02$. With the open circuit condition, the first three frequencies are 130.2167 Hz, 650.3930 Hz, and 1699.5167 Hz, as shown in Figure 3(a). Whereas, with the short-circuit condition, the frequencies are 65.1092 Hz, 325.2265 Hz, and 852.6257 Hz, respectively. The short-circuit natural frequencies are lower because the strong piezoelectric coupling effectively reduces stiffness. A fast convergence is observed for the first natural frequency, which is $\simeq$129.721 $\rightarrow$ 130.217 Hz as the mesh is refined, as shown in Figure 3(b). Most of the change is observed between 10 and 40 elements, whereas the change is $\lesssim 0.1\%$ beyond 80 elements, confirming the stability of the frequency. This indicates that the model's stiffness and mass integrals eventually, the eigenvalues are well captured even with a moderate mesh density.

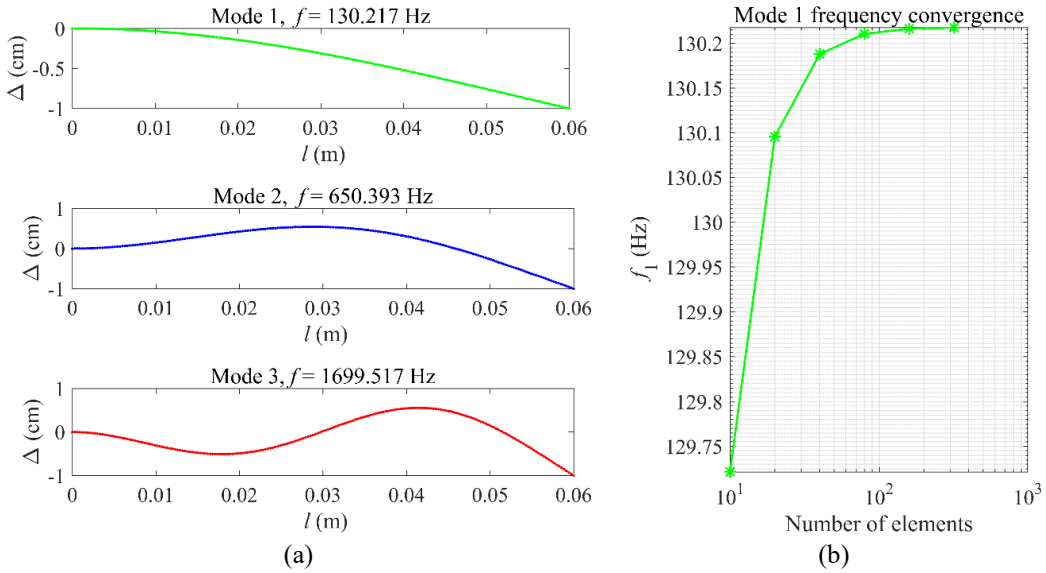

Figure 3. Modal analysis responses showing; (a) the first three mode shapes and (b) the mesh convergence result of the first natural frequency

3.2.2. Harmonic responses

A harvester model with configurations $l = 6$ cm, $\vartheta = 0.6$, $w_0 = 5$ cm, $h_s = 0.5$ mm, $h_p = 0.2$ mm, and $\zeta = 0.02$ is analyzed to obtain the voltage responses for the first three modes. The analysis is done for short-circuit ($R = 0$), open circuit ($R = \infty$), R =10^2, 10^3, 10^4, 10^5, and 10^6 Ω to get a clear understanding of the effect of the load resistance on the harvester's performance. Figure 4 shows the mode 1 voltage responses from the harvester under 1 g (Figure 4(a)), 4 g (Figure 4(b)), and 7 g (Figure 4(c)) accelerations. It is seen that the voltage response increases with an increase in the load resistance, having a peak at $R = \infty$. Also, the voltage response increases sharply with an increase in base excitation due to the availability of higher kinetic energy in the form of large level vibration. Similar trends are observed for modes 2 and 3. But the magnitude of the voltages at higher modes is insignificant compared to the first mode. To further understand the influence of the acceleration, surface plots are plotted for the voltage response against frequency and acceleration. Figure 5 shows the surface plots for an acceleration sweep of 1-7 g. The plots are drawn for mode 1 (Figure 5(a)), mode 2 (Figure 5(b)), and mode 3 (Figure 5(c)). It is clear that the voltage response is directly influenced by the acceleration level.

Harmonic analysis is also done for the RMS power response from the harvester. Since the voltage response at the first mode is significantly higher compared to the other two, the power is also calculated for the first mode only. Figure 6 shows the mode 1 RMS power responses from the harvester under 1 g (Figure 6(a)), 4 g (Figure 6(b)), and 7 g (Figure 6(c)) accelerations. It is seen that the power response increases with an increase in the load resistance, having a peak at $R = 10^6\ \Omega$. Also, the power response increases sharply with an increase in base excitation due to the availability of higher kinetic energy in the form of a large level vibration. Table 4 shows the peak voltage and power responses from the harvester across various resistive loads under 1 g, 4 g, and 7 g accelerations for the first mode. It is noticed that the voltage response from the harvester with 10^6 Ω is approaching the response under open circuit conditions.

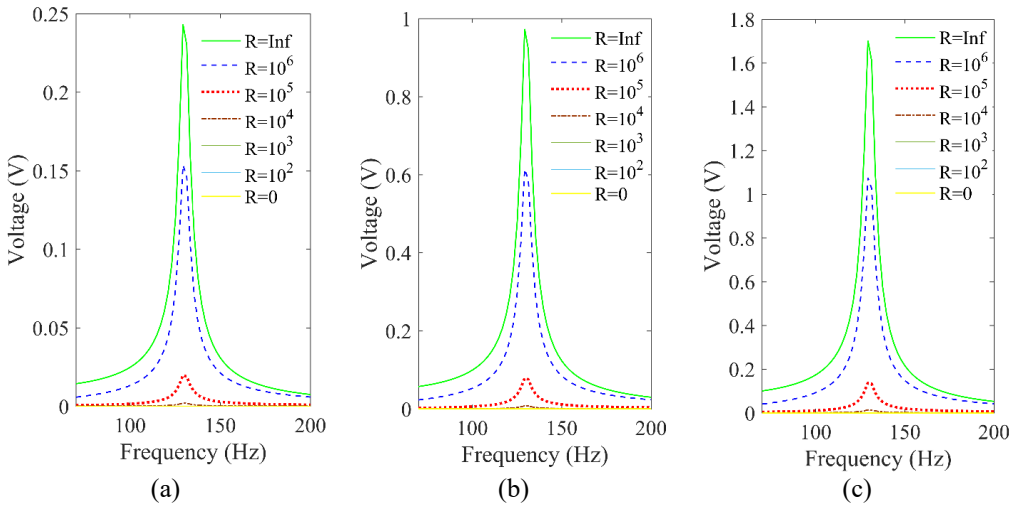

Figure 4. Voltage response from the harvester for mode 1 under various resistive loads for; (a) 1 g, (b) 4 g, and (c) 7 g accelerations

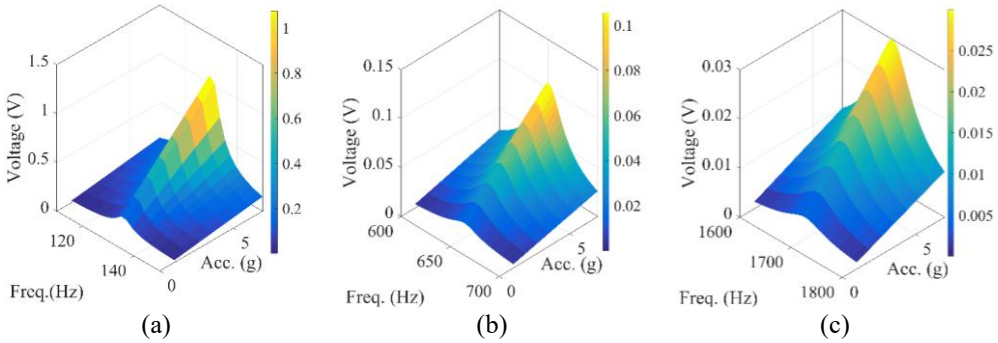

Figure 5. Surface plots for voltage response vs frequency and acceleration for mode; (a) 1, (b) 2, and (c) 3

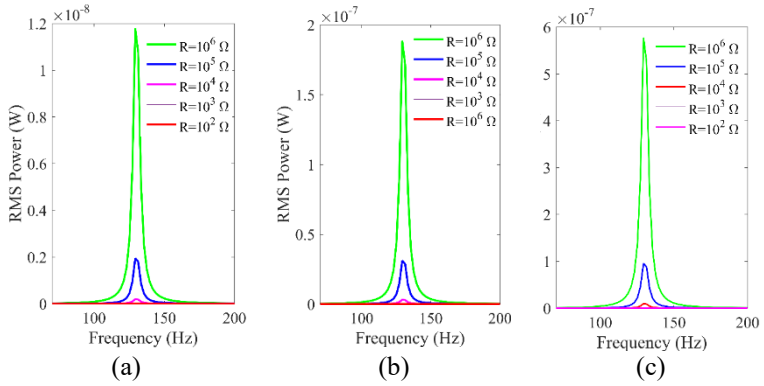

Figure 6. RMS power responses from the harvester across various load resistances under; (a) 1 g, (b) 4 g, and (c) 7 g accelerations

Table 4. Peak voltage and power responses from the harvester under 1 g, 4 g, and 7 g accelerations

Acc. level	Voltage response (V) and power responses (μW)							
	$R = 10^2\ \Omega$		$R = 10^4\ \Omega$		$R = 10^6\ \Omega$		$R = \infty\ \Omega$	
	Power	Voltage	Power	Voltage	Power	Voltage	Power	Voltage
1 g	1.9×10^6	0.00002	0.0002	0.00198	0.012	0.15357	-	0.24330
4 g	3.13×10^{-5}	0.00008	0.0031	0.00792	0.189	0.61430	-	0.97321
7 g	9.6×10^{-5}	0.00014	0.0096	0.01386	0.578	1.07502	-	1.70312

3.3. Parametric analysis

The taper parameter, harvester's length, and the piezoelectric layer thickness significantly influence the harvester's responses. Therefore, a parametric analysis is conducted to get a deep insight into the parameters' influence. Initially, the harvester with $l = 6$ cm, $w_0 = 5$ cm, $h_s = 0.5$ mm, $R = 10^6\ \Omega$, and $h_p = 0.2$ mm is studied for $\vartheta = 0.4, 0.6, and\ 0.8$ under 1 g excitation, as shown in Figure 7.

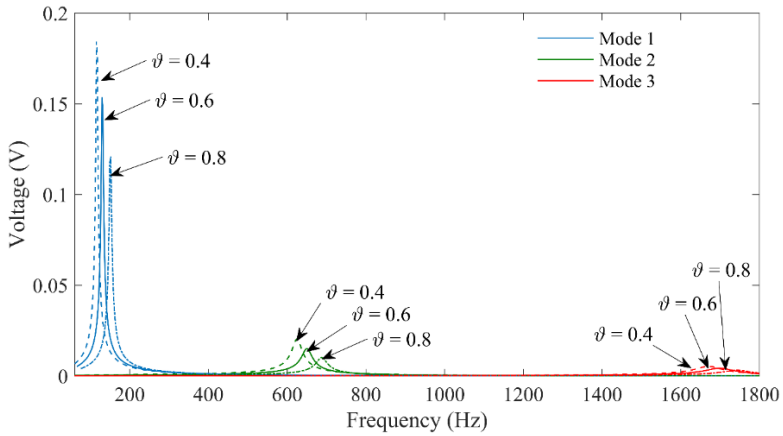

Figure 7. Voltage response for all three modes with various taper parameters under 1 g excitation

The voltage response decreases with an increase in taper parameter, and the resonance frequencies shift towards higher regions for all three modes. The earlier effect is the result of less availability of piezoelectric material to produce voltage with a higher taper, leading to a narrow geometry, which, on the other hand, increases the flexural rigidity of the system, leading to the frequency shift to higher values. The voltage decreases from 0.2822 V to 0.1931 V for the taper parameter change from 0.4 to 0.8. Figure 8 shows the effect of the harvester's length on its performance. The design parameters are $w_0 = 5\ cm, h_s = 0.5\ mm, R = 10^6\Omega, h_p = 0.2\ mm$, and $\vartheta = 0.6$ under 1 g excitation with $l = 5, 6, and\ 7\ cm$. It is observed that the voltage response increases with an increase in the harvester's length due to more availability of piezoelectric material. The voltage response increases from 0.1917 V to 0.3140 V when the harvester's length increases from 5 cm to 7 cm. Also, the natural frequencies shift to lower regions owing to the reduction in stiffness of longer beams.

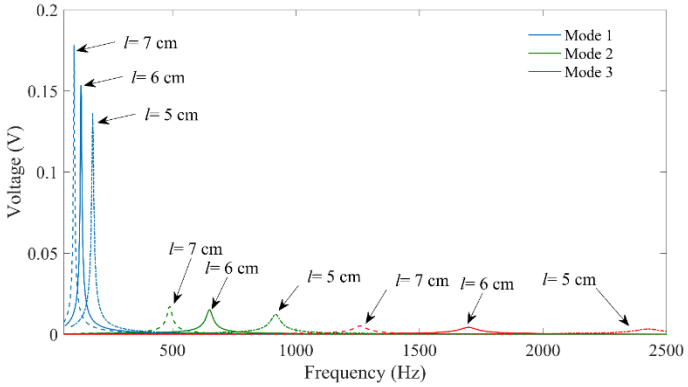

Figure 8. Voltage response for all the three modes with various harvester's length under 1 g excitation

The voltage response from the harvester with $l = 6\ cm, w_0 = 5\ cm, h_s = 0.5\ mm, R = 10^6\Omega$, and $\vartheta = 0.6$ is studied for $h_p = 0.1, 0.2, and\ 0.3\ mm$ as shown in Figure 9. It is clearly evident that the piezoelectric layer thickness has a significant influence on the voltage response but less on the frequency shift. The voltage response from the harvester increases from 0.0920 V to 0.5890 V when the thickness increases from 0.1 mm to 0.3 mm.

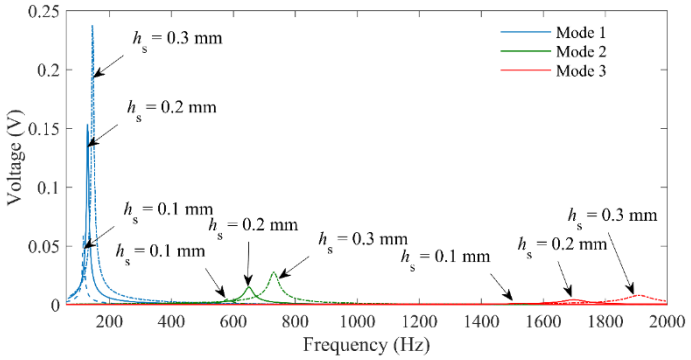

Figure 9. Voltage response for the three modes with various piezo layer thicknesses under 1 g excitation

Table 5 summarizes the effect of the electrical boundary condition under these parameter sweeps. It can be observed that the effects of the electrical boundary condition are independent of parameter sweep rather significantly depend on the piezoelectric material properties. Similarly, the comparison of modal frequency and voltage output under short-circuit, resistive, and open-circuit conditions for the parabolically tapered PEH shows that electrical loading influences effective stiffness, with open-circuit exhibiting the highest natural frequency.

Table 5. Short-circuit and open circuit first modal frequencies (Hz) for various parameter changes

Boundary conditions	Taper parameter			Harvester's length (cm)			Piezo layer thickness (mm)		
	$\vartheta = 0.4$	$\vartheta = 0.6$	$\vartheta = 0.8$	$l = 5$	$l = 6$	$l = 7$	$h_p = 0.1$	$h_p = 0.2$	$h_p = 0.3$
S-C	58.098	65.109	75.351	88.672	65.109	50.92	58.229	65.1092	73.176
O-C	115.29	130.21	150.69	177.3	130.21	101.8	116.45	130.217	145.36

4. CONCLUSION

A detailed analytical framework has been developed and validated for predicting the dynamic and electrical behavior of parabolically tapered piezoelectric vibration energy harvesters under multiple boundary conditions. The study integrates variable stiffness and mass effects, as well as the neutral-axis shift, into a one-dimensional coupled electromechanical model, enabling accurate computation of modal frequencies,

voltage, and power outputs. Comparison with ANSYS simulations confirms the validity of the proposed model, with less than 2% deviation in frequency and power predictions. The results clearly establish that while open-circuit conditions produce the highest voltage output, the maximum power occurs at a matched resistive load, consistent with impedance matching theory. Notably, under 7 g excitation, the PEH shows a peak open-circuit voltage of 1.70312 V and power of 0.578 μW. The O-C voltage response is observed to be 58.4% more compared to the voltage against $R = 10^6\,\Omega$.

The parametric analysis highlights the importance of the taper parameter, beam length, and piezoelectric layer thickness on system performance. Specifically, decreasing the taper parameter or increasing the beam length enhances voltage generation, whereas thicker piezoelectric layers amplify output power without significantly affecting resonance frequency. The parabolic taper provides superior strain distribution and improved electromechanical coupling compared to uniform or linearly tapered harvesters. Overall, this research presents a validated and scalable analytical approach for the design of high-performance, geometry-tailored PEHs, contributing to the development of efficient vibration-powered energy solutions for low-frequency ambient environments and wireless sensor networks.

FUNDING INFORMATION

Authors state no funding involved.

AUTHOR CONTRIBUTIONS STATEMENT

This journal uses the Contributor Roles Taxonomy (CRediT) to recognize individual author contributions, reduce authorship disputes, and facilitate collaboration.

Name of Author	C	M	So	Va	Fo	I	R	D	O	E	Vi	Su	P	Fu
Avipsa Priyadarshini	✓	✓	✓	✓	✓	✓		✓	✓	✓			✓	
Pramod Bakhati		✓	✓			✓		✓	✓		✓			
Shashank Shekhar Pradhan			✓	✓			✓				✓			
Ishan Gupta			✓	✓			✓				✓			
Rakesh Ranjan Chand	✓				✓		✓			✓		✓		✓

C : **C**onceptualization
M : **M**ethodology
So : **So**ftware
Va : **Va**lidation
Fo : **Fo**rmal analysis
I : **I**nvestigation
R : **R**esources
D : **D**ata Curation
O : Writing - **O**riginal Draft
E : Writing - Review & **E**diting
Vi : **Vi**sualization
Su : **Su**pervision
P : **P**roject administration
Fu : **Fu**nding acquisition

CONFLICT OF INTEREST STATEMENT

Authors state no conflict of interest.

DATA AVAILABILITY

The data that support the findings of this study are available from the corresponding author, upon reasonable request.

REFERENCES

[1] R. Shekhar and D. Mala, "A review on design and analysis of piezoelectric energy harvesting systems," *Intellectual Journal of Energy Harvesting and Storage*, vol. 1, no. 1, pp. 24–34, Jun. 2023, doi: 10.11591/ehs.v1i1.pp24-34.

[2] A. Erturk and D. J. Inman, "On mechanical modeling of cantilevered piezoelectric vibration energy harvesters," *Journal of Intelligent Material Systems and Structures*, vol. 19, no. 11, pp. 1311–1325, Nov. 2008, doi: 10.1177/1045389X07085639.

[3] R. Andosca *et al.*, "Experimental and theoretical studies on MEMS piezoelectric vibrational energy harvesters with mass loading," *Sensors and Actuators A: Physical*, vol. 178, pp. 76–87, May 2012, doi: 10.1016/j.sna.2012.02.028.

[4] Q. Xu, A. Gao, Y. Li, and Y. Jin, "Design and optimization of piezoelectric cantilever beam vibration energy harvester," *Micromachines*, vol. 13, no. 5, Apr. 2022, doi: 10.3390/mi13050675.

[5] S. E. Osheidu, C. Israel-Cookey, A. R. C. Amakiri, F. B. Sigalo, and O. A. Davies, "Analytical modelling of resistive load effect on transient voltage and power output from d_33-mode piezoelectric vibration energy harvester," *International Journal of Current Science Research and Review*, vol. 08, no. 01, pp. 278–286, Jan. 2025, doi: 10.47191/ijcsrr/V8-i1-30.

[6] Y.-H. Huang, Z. C. Ong, S.-L. Chou, and P. Y. Siow, "Resonant frequency reduction of piezoelectric vibration energy harvester by spring boundary condition," *Engineering Research Express*, vol. 7, no. 1, Mar. 2025, doi: 10.1088/2631-8695/ada726.

[7] B. Wang, X. Luo, Y. Liu, and Z. Yang, "Thickness-variable composite beams for vibration energy harvesting," *Composite Structures*, vol. 244, Jul. 2020, doi: 10.1016/j.compstruct.2020.112232.
[8] H. Salmani and G. H. Rahimi, "Study the effect of tapering on the nonlinear behavior of an exponentially varying width piezoelectric energy harvester," *Journal of Vibration and Acoustics*, vol. 140, no. 6, Dec. 2018, doi: 10.1115/1.4039932.
[9] R. R. Chand and A. Tyagi, "Parametric analysis of a rotational piezoelectric-coupled tapered-bimorph structure with various boundary conditions under transient axial loading," *Journal of Vibration Engineering & Technologies*, vol. 9, no. 5, pp. 907–917, Jul. 2021, doi: 10.1007/s42417-020-00272-9.
[10] A. Quattrocchi *et al.*, "A new approach for impedance tracking of piezoelectric vibration energy harvesters based on a zeta converter," *Sensors*, vol. 20, no. 20, Oct. 2020, doi: 10.3390/s20205862.
[11] A. Morel, A. Badel, R. Grézaud, P. Gasnier, G. Despesse, and G. Pillonnet, "Resistive and reactive loads' influences on highly coupled piezoelectric generators for wideband vibrations energy harvesting," *Journal of Intelligent Material Systems and Structures*, vol. 30, no. 3, pp. 386–399, Feb. 2019, doi: 10.1177/1045389X18810802.
[12] M. Zhu, E. Worthington, and J. Njuguna, "Analyses of power output of piezoelectric energy-harvesting devices directly connected to a load resistor using a coupled piezoelectric-circuit finite element method," *IEEE Transactions on Ultrasonics, Ferroelectrics, and Frequency Control*, vol. 56, no. 7, pp. 1309–1317, Jul. 2009, doi: 10.1109/TUFFC.2009.1187.
[13] A. N. Sevugan, H. Murugan, M. Ramamoorthy, and V. Rajamohan, "Modeling and analysis of tapered composite beams with piezoelectric energy harvester: Numerical and experimental investigations," *Mechanics Based Design of Structures and Machines*, vol. 52, no. 4, pp. 2173–2192, Apr. 2024, doi: 10.1080/15397734.2023.2172031.
[14] I. Djabrouhou, A. Mahieddine, S. Bentridi, K. M. Kouadria, and M. Hemis, "Dynamic behavior of unimorph FGPM tapered beam actuator subjected to electrical harmonic load," *Journal of Vibration Engineering & Technologies*, vol. 12, no. 2, pp. 2425–2435, Feb. 2024, doi: 10.1007/s42417-023-00988-4.
[15] D. S. Ibrahim, X. Shen, U. Javaid, U. Sharif, and O. O. Adewale, "Experimental-numerical analyses on energy harvesting characteristics of non-conventional T-shaped beams with varied piezoelectric patch location and anchor position," *Mechanics Based Design of Structures and Machines*, vol. 52, no. 11, pp. 8839–8864, Nov. 2024, doi: 10.1080/15397734.2024.2330652.
[16] A. Keshmiri and N. Wu, "Structural stability enhancement by nonlinear geometry design and piezoelectric layers," *Journal of Vibration and Control*, vol. 25, no. 3, pp. 695–710, Feb. 2019, doi: 10.1177/1077546318794540.
[17] L. Jin, S. Gao, X. Zhang, and Q. Wu, "Output of MEMS piezoelectric energy harvester of double-clamped beams with different width shapes," *Materials*, vol. 13, no. 10, May 2020, doi: 10.3390/ma13102330.
[18] C. V. Karadag, S. Ertarla, N. Topaloglu, and A. F. Okyar, "Optimization of beam profiles for improved piezoelectric energy harvesting efficiency," *Structural and Multidisciplinary Optimization*, vol. 63, no. 2, pp. 631–643, Feb. 2021, doi: 10.1007/s00158-020-02714-0.
[19] W. Yu-Jen, C. Tsung-Yi, and Y. Jui-Hsin, "Design and kinetic analysis of piezoelectric energy harvesters with self-adjusting resonant frequency," *Smart Materials and Structures*, vol. 26, no. 9, Sep. 2017, doi: 10.1088/1361-665X/aa7ad6.
[20] Y.-J. Wang, T.-Y. Chuang, and C. Lee, "Resonant frequency self-tunable piezoelectric cantilevers for energy harvesting and disturbing torque absorbing," *Sensors and Actuators A: Physical*, vol. 285, pp. 25–34, Jan. 2019, doi: 10.1016/j.sna.2018.10.043.
[21] L. Deng, J. Jiang, L. Zhou, D. Zhang, and Y. Fang, "Design and simulation of a frequency self-tuning vibration energy harvester for rotational applications," *Microsystem Technologies*, vol. 27, no. 7, pp. 2857–2862, Jul. 2021, doi: 10.1007/s00542-020-05064-5.
[22] H. Salmani, G. H. Rahimi, and S. A. Hosseini Kordkheili, "An exact analytical solution to exponentially tapered piezoelectric energy harvester," *Shock and Vibration*, vol. 2015, pp. 1–13, 2015, doi: 10.1155/2015/426876.
[23] R. R. Chand and A. Tyagi, "Design and experimental validation of an exponentially tapering width rotational piezoelectric vibration energy harvester," *Journal of Intelligent Material Systems and Structures*, vol. 34, no. 1, pp. 15–28, Jan. 2023, doi: 10.1177/1045389X221093315.
[24] R. R. Chand and A. Tyagi, "Parabolic tapering piezoelectric rotational energy harvester: Numerical analysis with experimental validation," *Mechanics of Advanced Materials and Structures*, vol. 30, no. 18, pp. 3652–3661, Sep. 2023, doi: 10.1080/15376494.2022.2080893.
[25] J. Baker, S. Roundy, and P. Wright, "Alternative geometries for increasing power density in vibration energy scavenging for wireless sensor networks," in *3rd International Energy Conversion Engineering Conference*, Aug. 2005, pp. 1–12, doi: 10.2514/6.2005-5617.
[26] R. R. Chand and A. Tyagi, "Investigation of the effects of the piezoelectric patch thickness and tapering on the nonlinearity of a parabolic converging width vibration energy harvester," *Journal of Vibration Engineering & Technologies*, vol. 10, no. 1, pp. 1–18, Jan. 2022, doi: 10.1007/s42417-021-00359-x.
[27] S. P. Joshi, "Non-linear constitutive relations for piezoceramic materials," *Smart Materials and Structures*, vol. 1, no. 1, pp. 80–83, Mar. 1992, doi: 10.1088/0964-1726/1/1/012.
[28] A. Abdelkefi, A. H. Nayfeh, and M. R. Hajj, "Effects of nonlinear piezoelectric coupling on energy harvesters under direct excitation," *Nonlinear Dynamics*, vol. 67, no. 2, pp. 1221–1232, Jan. 2012, doi: 10.1007/s11071-011-0064-9.
[29] K. Morimoto, I. Kanno, K. Wasa, and H. Kotera, "High-efficiency piezoelectric energy harvesters of c-axis-oriented epitaxial PZT films transferred onto stainless steel cantilevers," *Sensors and Actuators A: Physical*, vol. 163, no. 1, pp. 428–432, Sep. 2010, doi: 10.1016/j.sna.2010.06.028.
[30] G. Tang *et al.*, "A piezoelectric micro generator worked at low frequency and high acceleration based on PZT and phosphor bronze bonding," *Scientific Reports*, vol. 6, no. 1, Dec. 2016, doi: 10.1038/srep38798.
[31] H.-C. Song *et al.*, "Ultra-low resonant piezoelectric MEMS energy harvester with high power density," *Journal of Microelectromechanical Systems*, vol. 26, no. 6, pp. 1226–1234, Dec. 2017, doi: 10.1109/JMEMS.2017.2728821.
[32] M. Kim, M. Hoegen, J. Dugundji, and B. L. Wardle, "Modeling and experimental verification of proof mass effects on vibration energy harvester performance," *Smart Materials and Structures*, vol. 19, no. 4, Apr. 2010, doi: 10.1088/0964-1726/19/4/045023.
[33] J. Liang and W.-H. Liao, "Impedance matching for improving piezoelectric energy harvesting systems," in *Proceedings of SPIE - The International Society for Optical Engineering*, Mar. 2010, pp. 76430K-1-76430K–12, doi: 10.1117/12.847524.
[34] C. Xu *et al.*, "Cantilever driving low frequency piezoelectric energy harvester using single crystal material 0.71Pb(Mg1/3Nb2/3)O3-0.29PbTiO3," *Applied Physics Letters*, vol. 101, no. 3, Jul. 2012, doi: 10.1063/1.4737170.
[35] M. Ma, S. Xia, Z. Li, Z. Xu, and X. Yao, "Enhanced energy harvesting performance of the piezoelectric unimorph with perpendicular electrodes," *Applied Physics Letters*, vol. 105, no. 4, Jul. 2014, doi: 10.1063/1.4891851.
[36] L. J. Gong, Q. S. Pan, W. Li, G. Y. Yan, Y. Bin Liu, and Z. H. Feng, "Harvesting vibration energy using two modal vibrations of a folded piezoelectric device," *Applied Physics Letters*, vol. 107, no. 3, Jul. 2015, doi: 10.1063/1.4927331.